Effects of non-equilibrium angle fluctuation on F_1-ATPase kinetics induced by temperature increase

Yuji Tamiya, Rikiya Watanabe, Hiroyuki Noji, Chun-Biu Li, Tamiki Komatsuzaki

Supplemental Information

More Details of the Model Settings and Numerical Calculation

In the simulation, we used the overdamped Langevin equation of the rotary angle θ with stochastically switching harmonic potentials;

$$\Gamma\frac{d\theta}{dt} = -\frac{dG^{\mathrm{pre/post}}(\theta)}{d\theta} + \sqrt{2\Gamma k_B T}\xi(t), \tag{S.1}$$

where Γ is the effective friction constant against the probe and $\xi(t)$ the Gaussian white noise. The free energy potential is as follows;

$$G^{(\mathrm{pre/post})}(\theta) = \begin{cases} \frac{\kappa}{2}(\theta-\theta_0^{\mathrm{pre/post}})^2 & |\theta-\theta_0^{\mathrm{pre/post}}| < \theta_c \\ T_\theta(\theta-\theta_c-\theta_0^{\mathrm{pre/post}}) + \frac{\kappa}{2}(\theta_c-\theta_0^{\mathrm{pre/post}})^2 & \theta-\theta_0^{\mathrm{pre/post}} > \theta_c \\ -T_\theta(\theta+\theta_c-\theta_0^{\mathrm{pre/post}}) + \frac{\kappa}{2}(\theta_c-\theta_0^{\mathrm{pre/post}})^2 & \theta-\theta_0^{\mathrm{pre/post}} < -\theta_c. \end{cases} \tag{S.2}$$

$\theta_0^{\mathrm{pre/post}}$ is the center of the potential with -10° for pre-hydrolysis dwell and 10° for post-hydrolysis dwell. It is basically a harmonic potential and the value of its curvature $\kappa = 1.62\times10^{-2}$ pN nm deg.$^{-2}$ was determined in the previous result[1] so that the dwell angle distribution width during a whole catalytic dwell coincides with that of the experiment. In the outer region ($|\theta-\theta_0^{\mathrm{pre/post}}| > \theta_c$) the potential form is smoothly connected to linear ones so that its maximum torque $|dG/d\theta|$ equals to the experimental value $T_\theta = 0.70$ pN nm deg.$^{-1}$ (=40 pN nm rad.$^{-1}$).[2,3] The cut-off point $\theta_c = 43.1°$ is where the harmonic potential slope coincides with this value; $\kappa(\theta_c-\theta_0) = T_\theta$.

While we numerically solved the Langevin equation (S.1) by Heun method[4] with 1st order precision, for each simulation time step $t \to t+\Delta t$ we calculated the transition probability $P_{\mathrm{tr}}^{(i)}(t) = 1-\exp\left\{-\int_t^{t+\Delta t} k_i(\theta(t'))dt'\right\} (\approx k_i(\theta(t))\Delta t)$ to determine whether or not to switch the potential with the Monte-Carlo method.

Non-equilibrium Angle Distribution

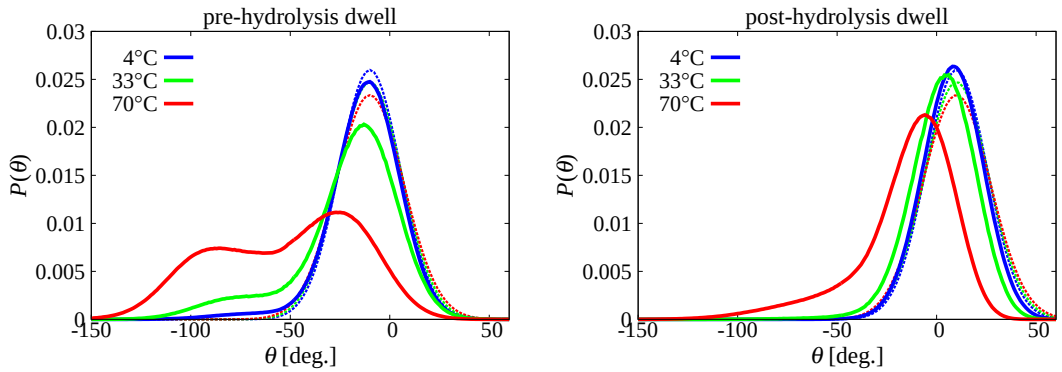

(a) (b)

Fig.S1: Steady state angle distributions in pre- and post-hydrolysis dwells obtained from model simulations (solid lines, blue : 4°C, green : 33°C, red : 70°C). As the temperature gets higher, the angle distributions deviate from the local-equilibrium distributions (broken curves), shifting toward the small angle region.

The steady state angle distributions during pre- and post-hydrolysis dwells are shown in Fig. S1 with the corresponding local-equilibrium distribution $P^{\rm eq}_{\rm pre/post}(\theta;T)$ (broken curve) at 4, 33, 70°C. Here we calculated the local-equilibrium distribution from the Boltzmann distribution using the free energy potential $G^{\rm pre/post}(\theta)$; $P^{\rm eq.}_{\rm pre/post}(\theta;T) \propto \exp\{-G^{\rm pre/post}(\theta)/k_BT\}$ while the steady state distribution was constructed from the rotary angle during the whole catalytic dwells in a single simulation time series.

Parameter Determination of the Angle-Dependent Rate Constants

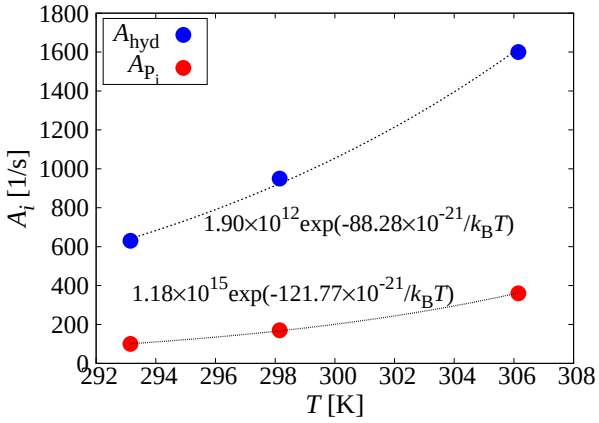

Fig.S2: Relationship between temperature T and the tuned parameter A_i for the angle-dependent rate constants of hydrolysis (blue circles) and P_i release (red circles). By fitting them with exponential functions, we determined pre-factors ν_i and average activation free energies ε_i so that $A_i(T) = \nu_i e^{-\varepsilon_i/k_BT}$.

Table.S1: Simulation parameters for angle-dependent rate constants

	α_i [pN·nm·deg.$^{-1}$]	ν_i [1/s]	ε_i [pN·nm] ([kJ/mol])
Hydrolysis	0.078	1.90×10^{12}	88.28 (53.16)
P_i release	0.47	1.18×10^{15}	121.8 (73.33)

From the experimentally-obtained values of rate coefficients, we determined the angle-dependent rate constants for simulation;

$$k_i(\theta;T) = \nu_i \exp\left\{-\frac{1}{k_BT}\left(\varepsilon_i - \alpha_i\theta\right)\right\}. \tag{S.3}$$

First, we set them as

$$k_i(\theta;T) = A_i e^{\alpha_i\theta/k_BT}, \tag{S.4}$$

where angle-dependent coefficients α_i were taken from stall-and-release experiments $k_i(\theta) \propto e^{b_i\theta}$, where $b_i(=\alpha_i/k_BT)$ at 23°C were 0.019, 0.12 deg.$^{-1}$ for hydrolysis and P_i release, respectively.[5] Next, we ran the simulation and searched for the appropriate values of A_i to reproduce the rate coefficients (averaged among samples) at each temperature $(16, 20, 25, 33°C)$. From the temperature dependence of tuned values A_i, we separated out the prefactors and the averaged activation free energy, assuming $A_i(T) = \nu_i e^{-\varepsilon_i/k_BT}$ (Fig. S2). The obtained values are shown in Table. S1.

Determination of Effective Friction Constant

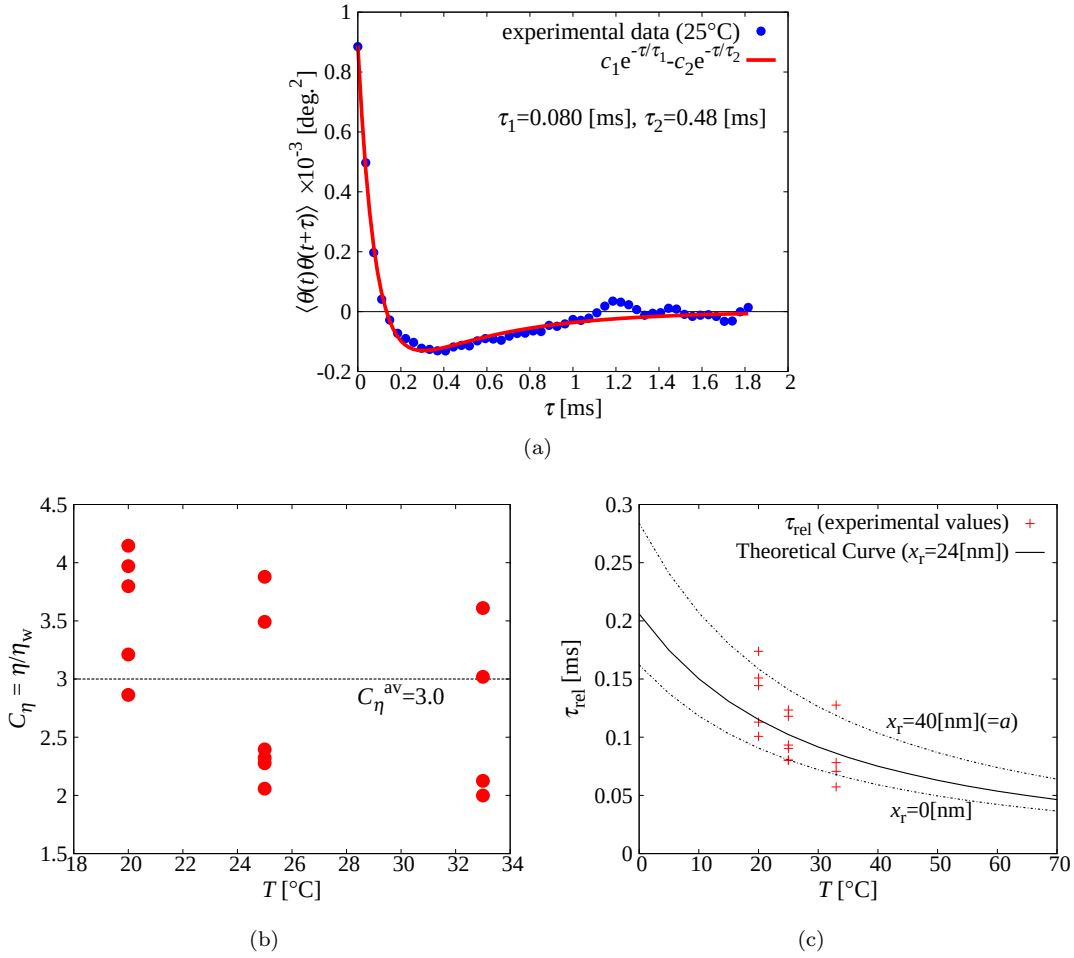

Fig.S3: (a) The autocorrelation function of the rotary angle during a catalytic dwell of the experimental rotation time series at 25°C. In the calculation, we subtracted the linear trend to take into account the small angle shift after hydrolysis. It can be fitted with a double exponential function $c_1e^{\tau/\tau_1} - c_2e^{\tau/\tau_2}$, where we regard the faster timescale τ_1 as the relaxation time $\tau_{\rm rel} = \Gamma/\kappa$. (b) The proportionality of the viscosity of the media against that of water for each time series. The values C_η are estimated from the relaxation time and eq.(S.5), using the revolution radii $x_{\rm r}$ measured from the rotary traces. (c) The relationship between temperature T and experimentally observed relaxation time $\tau_{\rm rel}$ (red points) with theoretical curves using the average value of the proportionality constant $C_\eta^{\rm av} = 3.0$. While the black curve shows the theoretical values with the average revolution radius $x_{\rm r} = 24$ nm, the region within dash curves shows those of $x_{\rm r} = 0 \sim 40$ nm (= bead radius a).

Theoretically, the effective friction constant against a probe bead revolving around a fixed axis can be calculated by fluid mechanics[6] as

$$\Gamma = (8\pi a^3 + 6\pi a x_{\rm r}^2)\eta(T), \tag{S.5}$$

where a, $x_{\rm r}$, and $\eta(T)$ denote the bead radius, the revolution radius, and the temperature (T)-dependent viscosity of the media, respectively. While $a = 40$ nm and $x_{\rm r}$ can be obtained from rotary traces (24 nm on average), we do not know the viscosity of the media $\eta(T)$. Here, we assumed that $\eta(T)$ is linearly proportional to the water viscosity $\eta_{\rm w}(T)$ and estimated its temperature-independent constant of proportionality C_η , i.e., $\eta(T) = C_\eta \eta_{\rm w}(T)$, from the auto-correlation relaxation time.

We calculated the auto-correlation function of the rotary angle during a catalytic dwell, where we subtracted the linear trend due to the small rotation at hydrolysis.[1] In the over-damped Langevin system in a single harmonic potential $\frac{1}{2}\kappa\theta^2$, the auto-correlation function of the coordinate decays with

$$\langle \theta(t)\theta(t+\tau)\rangle \propto e^{-\tau/\tau_{\rm rel}}, \tag{S.6}$$

where $\langle\cdot\rangle$ is an ensemble average and $\tau_{\rm rel} = \Gamma/\kappa$. On the other hand, the real time series had two time constants (Fig. S3(a)). While we regarded the faster one as the relaxation time $\tau_{\rm rel}$, we ascribed the origin of the slower one to the small rotation after ATP hydrolysis during the catalytic dwell.[1] In fact, in simulation the second exponent appeared only when we incorporated the 20° angle shift between the pre- and post-hydrolysis potential wells.

Assuming that $\tau_{\rm rel}$ obtained above is also equal to Γ/κ and using the relation (S.5) with $\eta(T) = C_\eta \eta_{\rm w}(T)$, we obtained C_η for each time series (Fig.S3(b)). Although they have a small variation and still seem to show slight temperature dependence, we adopted their average value $C_\eta^{\rm av} = 3.0$ in the simulation because the resulting theoretical curve well reproduces the experimental values within a certain range (Fig.S3(c)) and the possible source of the variation can be due to the revolution radius fluctuation during rotary dwells. The cause of the three-times difference in viscosity between pure water and the media can be hydrodynamical effect near the glass surface.[7]

The Second Peak of the Steady State Angle Distribution in Pre-Hydrolysis Dwells

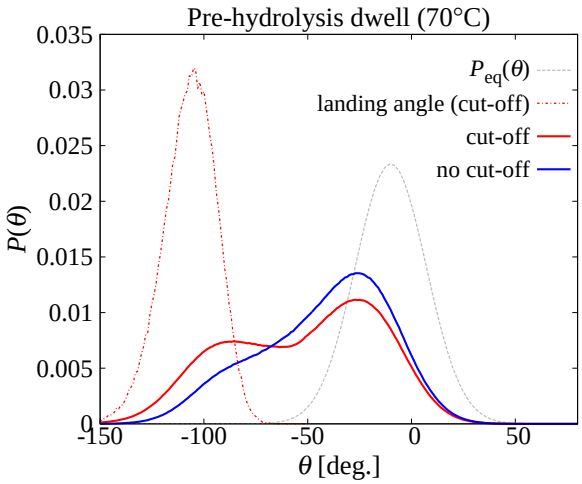

Fig.S4: The comparison of steady state angle distributions during the pre-hydrolysis dwell between with two types of potential forms; one introducing straight cut-offs at the outer edges (red curve) and a simple quadratic one (blue curve). Because the (mean) potential force $dG^{\rm pre}(\theta)/d\theta$ is weaker than that of the pure-quadratic one when $\theta < -53.1°$, the steady state angle distribution of the cut-off potential simulation has an artificial second bump at the smaller angle region $\sim -100°$. As a reference to show that the bump is a reminiscent of the initial distribution, the landing angle distribution, the angle at which the system lands into a pre-hydrolysis dwell, is also plotted (red broken curve), which relaxes toward the local-equilibrium distribution (grey broken curve).

At higher temperature around $50 \sim 70°$C, the steady state angle distribution in the pre-hydrolysis dwell has two peaks (Fig.S1). We have to remark here that the second peak around the small angle region $\sim -100°$ is an artifact due to the modified slope of the potential. As we wrote in the first section of this SI, the potential form is modified from a simple quadratic one and has constant slopes at the outer region so that the maximum torque does not exceed the experimental value.[3] This means that the mean potential force exerted just after landing on a pre-hydrolysis potential is weaker than that of a simple harmonic potential. Comparing the steady state angle distribution in the pre-hydrolysis dwell with that of a pure harmonic potential, the second peak around $\sim -100°$ is much smaller and almost indiscernible in the latter case (Fig.S4). This shows that the second peak for the modified potential is due to the slower rolling down of the potential after landing caused by the weaker power stroke force.

The Relationship between the Pearson Correlation Coefficient and 2D Correlation Plot

The two-body correlation $C(x, y)$ between two variables x and y is defined as below;

$$C(x, y) = P(x, y) - P(x)P(y), \tag{S.7}$$

where $P(x)$ is the probability density distribution of x and $P(x, y)$ is the joint probability of x and y. When x and y are independent, $P(x, y) = P(x)P(y)$ and $C(x, y) = 0$. Remark here that $\int\int C(x, y)dxdy = 0$.

On the other hand, the Pearson correlation coefficient C_{xy} between (x, y) is defined as below;

$$C_{xy} = \frac{\sigma_{xy}}{\sigma_x \sigma_y}, \tag{S.8}$$

where σ_x is the standard deviation of x and σ_{xy} is the covariance between x and y. σ_{xy} can be written as below;

$$\begin{aligned}
\sigma_{xy} &= \int\int (x - \bar{x})(y - \bar{y})P(x, y)dxdy - \int (x - \bar{x})P(x)dx \int (y - \bar{y})P(y)dy \\
&= \int\int (x - \bar{x})(y - \bar{y})P(x, y)dxdy - \int\int (x - \bar{x})(y - \bar{y})P(x)P(y)dxdy \\
&= \int\int (x - \bar{x})(y - \bar{y})C(x, y)dxdy,
\end{aligned} \tag{S.9}$$

where $\bar{x}$ is the average of x, $\int xP(x)dx$.

When (x, y) are a data set $(\{x_i, y_i\})$ $\quad i = 1, 2, ..., N$, C_{xy} is calculated as follows;

$$C_{xy} = \frac{\frac{1}{N-1}\sum_i^N (x_i - \bar{x})(y_i - \bar{y})}{\sqrt{\frac{1}{N-1}\sum_i^N (x_i - \bar{x})^2}\sqrt{\frac{1}{N-1}\sum_i^N (y_i - \bar{y})^2}}. \tag{S.10}$$

Meanwhile, in order to calculate $C(x, y)$ from the data set $(\{x_i, y_i\})$, we need $P(x), P(y)$, and $P(x, y)$, which we could obtain by determining the bin size and counting the number of the data in each bin. However, we have to be careful about the sampling error difference between $P(x, y)$ and $P(x)P(y)$ because the error can be larger in the former case even with the same sampling number because we need two-dimensional bins to calculate it, decreasing the number of the data in each bin. In order to make the data number in each bin the same and balance this sampling error difference, we also calculated $P(x)P(y)$ with two-dimensional bins, randomly shuffling the pairing of the data set $(\{x_i\}, \{y_i\})$ to cancel out the correlation.

2D Correlations of Post-Hydrolysis Dwell Time and the Next Pre-Hydrolysis Dwell Time

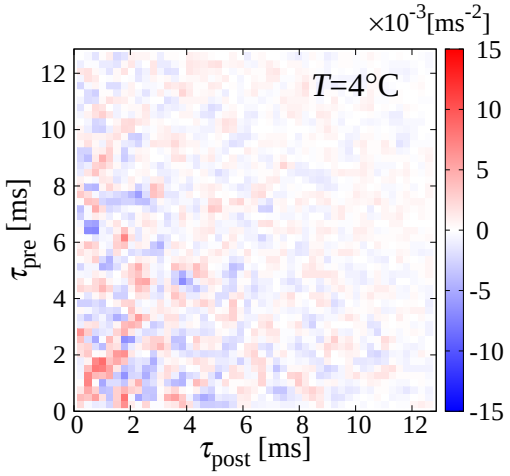

(a)

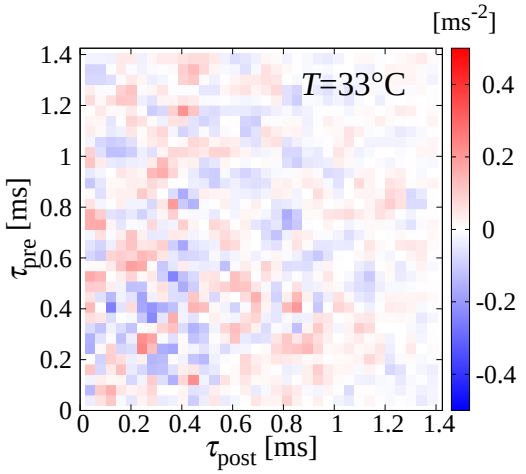

(b)

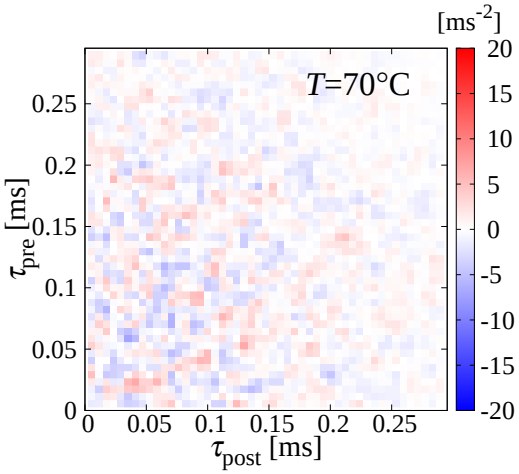

(c)

Fig.S5: The 2D correlation of the post-hydrolysis dwell time and the next pre-hydrolysis dwell time accompanied by 100° rotation (corresponding to Fig. 3(a) red line). The same as Fig. 3(b) ∼ (d), the two-body correlations $C(\tau_{\rm post}, \tau_{\rm pre})$ were plotted on 2D planes for 4(a), 33(b), 70(c)°C with a blue (smaller correlation) and red (larger) color scale. They show no consistent pattern, which suggests that $\tau_{\rm post}$ and its successive $\tau_{\rm pre}$ are almost independent.

While the negative sub-dwell time correlation between hydrolysis and P_i release during a catalytic dwell is pronounced as temperature increases (blue curve in Fig. 3(a)), P_i release waiting time and the next hydrolysis waiting time were not distinctly correlated with each other (red line in Fig. 3(a)). To see

more detail of this result, we also plotted in Fig.S5 the 2D correlation graph in the same way as Fig.3(b) $\sim$ (d). In these graphs, there are almost no consistent patterns over the τ_{post}-τ_{pre} planes. This assures our claim that the dwell time correlation is lost during a 100° power stroke rotation.

Deviation from a Double Exponential Fitting Function

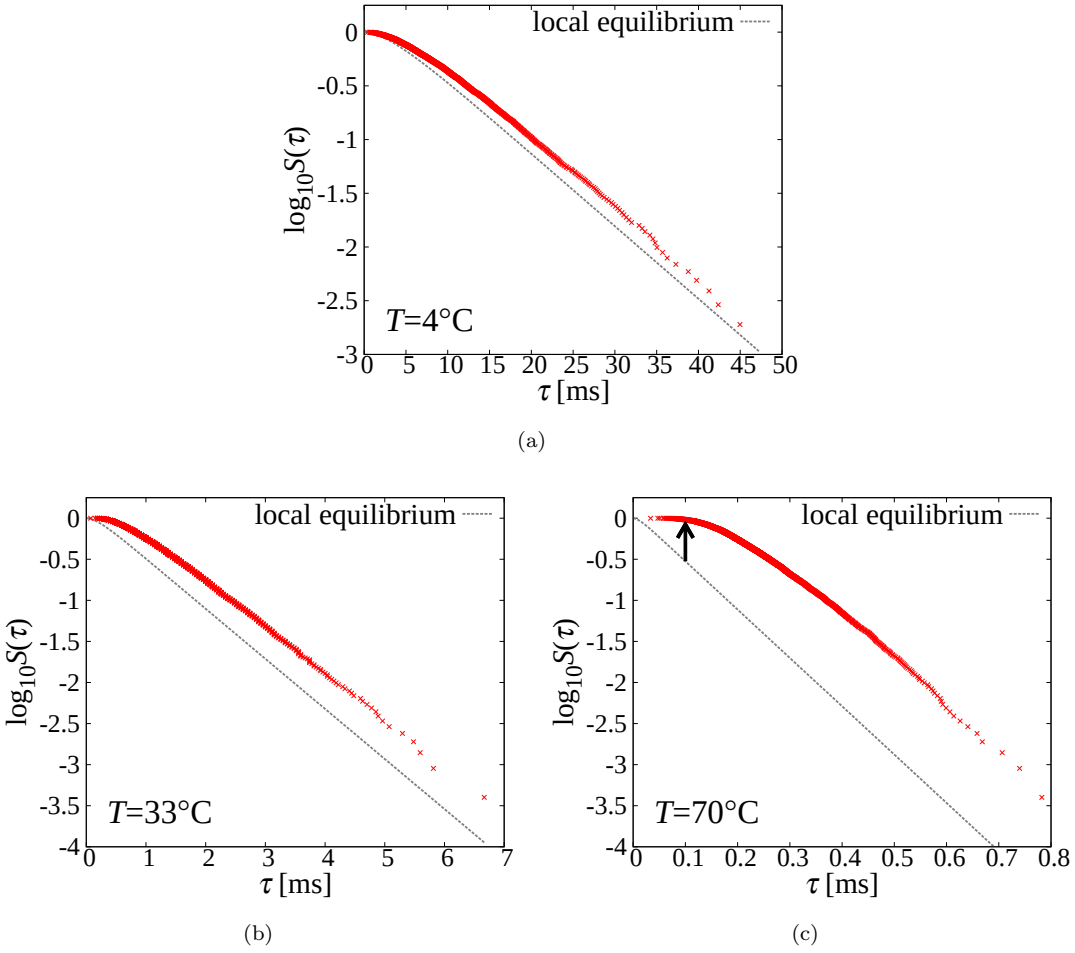

(a)

(b)

(c)

Fig.S6: The dwell time survival distributions at 4, 33, 70°C obtained by simulation (red). The grey broken lines shows double exponential functions assuming fast diffusion limit $\bar{k}^{FDL}_{\mathrm{hyd/P_i}}$, i.e., the steady-state angle distributions equal to the Boltzmann distributions.

The existence of correlation between pre- and post-hydrolysis dwell time in a catalytic dwell can in general introduce multiple (> 2) exponentials for the dwell time distribution. It may therefore invalidate the fitting we performed at temperature $T = 20, 25, 33$°C.

Fig. S6 shows the dwell time survival distributions at three different temperature (red dots, $T = 4, 33, 70$°C). In addition to the simulation data points, we also drew hypothetical distributions assuming the fast diffusion limit at both hydrolysis and $\mathrm{P_i}$ release (grey broken lines) in order to show how the functional form deforms as the temperature rises. The dwell time distributions show larger deviation from the fast diffusion limit at the higher T around $60 \sim 70$°C. The remarkable point is how they deviate; the shorter dwell time regions around the hydrolysis timescale $\langle \tau_{\mathrm{hyd}} \rangle_{\mathrm{FDL}}$ ($\simeq 6.4$ ms (4°C), 0.71

ms (33°C), 7.4×10^{-2} ms (70°C)) show larger deviation from the fast diffusion limit lines while the longer dwell time regions are almost parallel to them at three temperature. This suggests that the dominant cause of the deviation is the flattening of the survival distribution around the shorter dwell time region. We interpret that this suppression of shorter dwell time population to deform the dwell time distribution from a double exponential form is partly due to the negative correlation between the pre-hydrolysis dwell time (τ_{pre}) and the next post-hydrolysis dwell time (τ_{post}) observed as the temperature increases.

References

1 C.-B. Li, H. Ueno, R. Watanabe, H. Noji and T. Komatsuzaki, *Nature Communications*, 2015, **6**, 10223.

2 K. Hayashi, H. Ueno, R. Iino and H. Noji, *Physical Review Letters*, 2010, **104**, 218103.

3 R. Watanabe, K. Hayashi, H. Ueno and H. Noji, *Biophysical Journal*, 2013, **105**, 2385–2391.

4 P. E. Kloeden and E. Platen, *Numerical solution of stochastic differential equations*, Springer-Verlag, 1995.

5 R. Watanabe, R. Iino and H. Noji, *Nature chemical biology*, 2010, **6**, 814–820.

6 R. Yasuda, H. Noji, M. Yoshida, K. Kinosita and H. Itoh, *Nature*, 2001, **410**, 898–904.

7 H. Brenner, *Chemical Engineering Science*, 1961, **16**, 242–251.